CHAPTER – 8

High pressure torsion of the Ti-Zr-Nb-Mo-Fe-Cr based bio-CCA

8.1 Background

In recent years, high-entropy alloys (HEAs) or complex concentrated alloys (CCAs) have attracted significant attention in the field of biomedical applications due to their high strength and hardness, outstanding corrosion and wear resistance, and favorable cytocompatibility [64,218]. However, the elastic modulus of many reported CCAs remains significantly higher than that of cortical bone [67,69,75,232]. In Chapter 5, the as-cast and annealed $Ti_{35}Zr_{35}Nb_{15}Mo_5Fe_5Cr_5$ CCA exhibited elastic modulus values ranging from 97 GPa to 115 GPa. Although these values are notably lower than those of other bio-HEAs/CCAs reported in the literature, they are still higher than that of human cortical bone. Therefore, in this chapter, additional processing methods were explored to reduce the elastic modulus, with high-pressure torsion (HPT) identified as a promising technique to achieve this objective.

HPT is a severe plastic deformation technique used to tailor the microstructure of alloys to fine or even nanocrystalline grain sizes [96]. In addition, it introduces lattice defects such as vacancies and dislocations, which can lead to a significant reduction in the elastic modulus of the alloys [75,77,233]. For instance, Edalati et al. reported a notable decrease in the elastic modulus of HPT-deformed TiAlFeCoNi HEA from 254 GPa to 123 GPa [75]. Similarly, Maity et al. observed a decrease in the elastic modulus of the TiNbZrTa alloy from 73 GPa to 68 GPa with an increasing number of HPT turns [234]. In addition to the elastic modulus, HPT processing can also enhance the corrosion resistance and biocompatibility of HEAs as a result of microstructural modifications [75, 235-236].

Based on the aforementioned background, the aim of this chapter is to investigate the effect of HPT on the microstructure, mechanical response, corrosion behavior, and

biocompatibility of the $Ti_{35}Zr_{35}Nb_{15}Mo_5Fe_5Cr_5$ bio-CCA introduced in Chapter 5. The results presented in the current chapter are divided into four subsections. The first subsection presents the microstructural characterization of the HPT-deformed CCA. The second subsection examines its mechanical response. The third subsection evaluates the corrosion behaviour, and finally, the fourth subsection discusses the evolution of biocompatibility in the HPT-deformed CCA.

8.2 Results

8.2.1 Microstructural characterization of the HPT-deformed bio-CCA

The structural characterization of the HPT-deformed specimens was carried out using XRD to assess the evolution of the crystal structure. Figure 8.1 (a) exhibits the XRD patterns of the $Ti_{35}Zr_{35}Nb_{15}Mo_5Fe_5Cr_5$ CCA subjected to a varying number of HPT turns. As evident from the XRD patterns, all samples show two BCC solid solution phases along with a $TiCr_2$-type Laves phase. Notably, no new phases are formed as a result of the HPT process. However, with increasing HPT turns, a significant decrease in peak intensities and noticeable peak broadening is observed. This broadening is typically attributed to a reduction in crystallite size, the development of dislocations, and increased lattice strain [237].

The variation of average crystallite size (d), lattice strain (ε), and dislocation density (ρ) with the number of HPT turns are shown in Figure 8.1 (b). With an increasing number of HPT turns, the crystallite size significantly reduces from 25.74 ± 1.68 to 8.29 ± 1.10 nm. In contrast, lattice strain increases from 4.36×10^{-3} to 10.32×10^{-3} ($\pm 0.6 \times 10^{-3}$), and the dislocation density increases from 3.21×10^{15} to 17.50×10^{15} /m^2 ($\pm 1 \times 10^{15}$ /m^2).

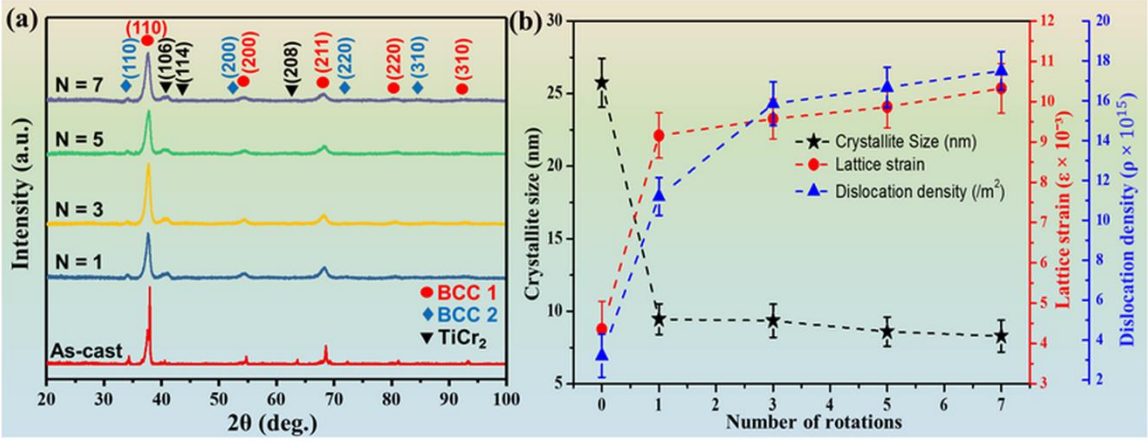

Figure 8.1 (a) X-ray diffraction pattern of the HPT-deformed specimens at various number of turns, (b) variation of average crystallite size, lattice strain, and dislocation density as a function of number of HPT turns.

Apart from the phases obtained in the XRD patterns, another phase was detected through TEM in the 7 turns HPT-deformed specimen. Analysis of the TEM bright-field image and the corresponding selected area diffraction (SAD) pattern shown in Figure 8.2 (a and b) indicates the formation of an FCC phase oriented along the $[\bar{2}33]$ zone axis as a result of the HPT deformation. In addition, the presence of superlattice reflections suggests a degree of ordering within the FCC structure, likely chemical in nature. This ordering appears to arise along the ⟨313⟩ direction due to multi-element interactions during HPT. However, this phase was not observed in the XRD analysis, possibly due to its very low volume fraction.

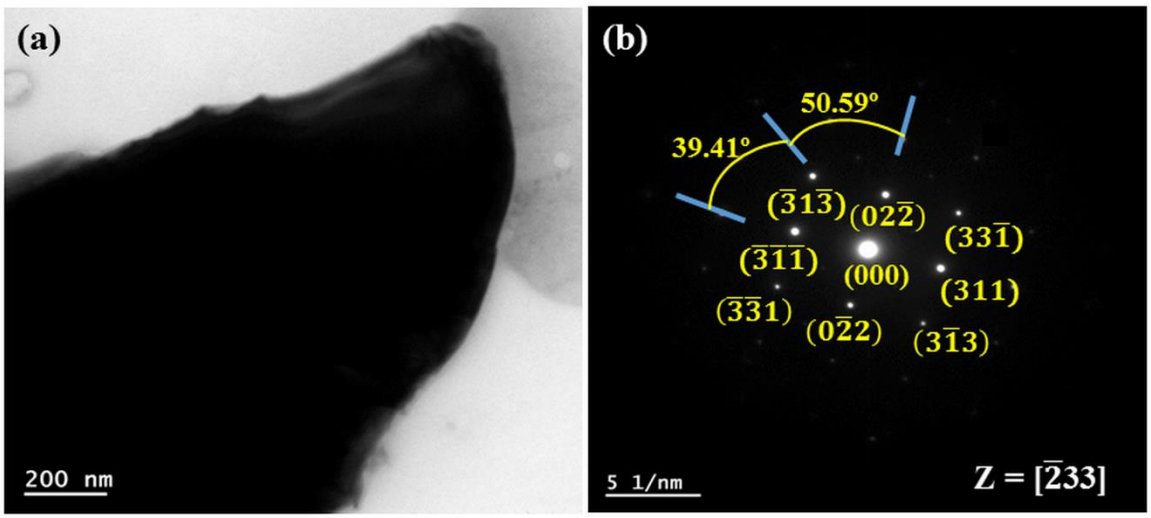

Figure 8.2 (a and b) TEM bright field image and the corresponding selected area diffraction (SAD) pattern from a 7-turns HPT-deformed $Ti_{35}Zr_{35}Nb_{15}Mo_5Fe_5Cr_5$ CCA specimen.

Figure 8.3 (a-d) shows SEM images along with the corresponding EDS elemental maps of the CCA subjected to various numbers of HPT rotations. As seen in Figure 8.3, increasing the number of rotations leads to progressive grain refinement and a more uniform elemental distribution. After one turn (Figure 8.3 (a) and its corresponding elemental mapping), higher melting elements like Mo and Nb are concentrated in dendritic regions, whereas lower-melting elements such as Fe and Cr are enriched in interdendritic areas. However, as the number of HPT turns increases, the elemental distribution becomes more uniform. Notably, the sample deformed up to 7 turns (Figure 8.3 (d)) exhibits a distinctly homogeneous distribution of constituent elements.

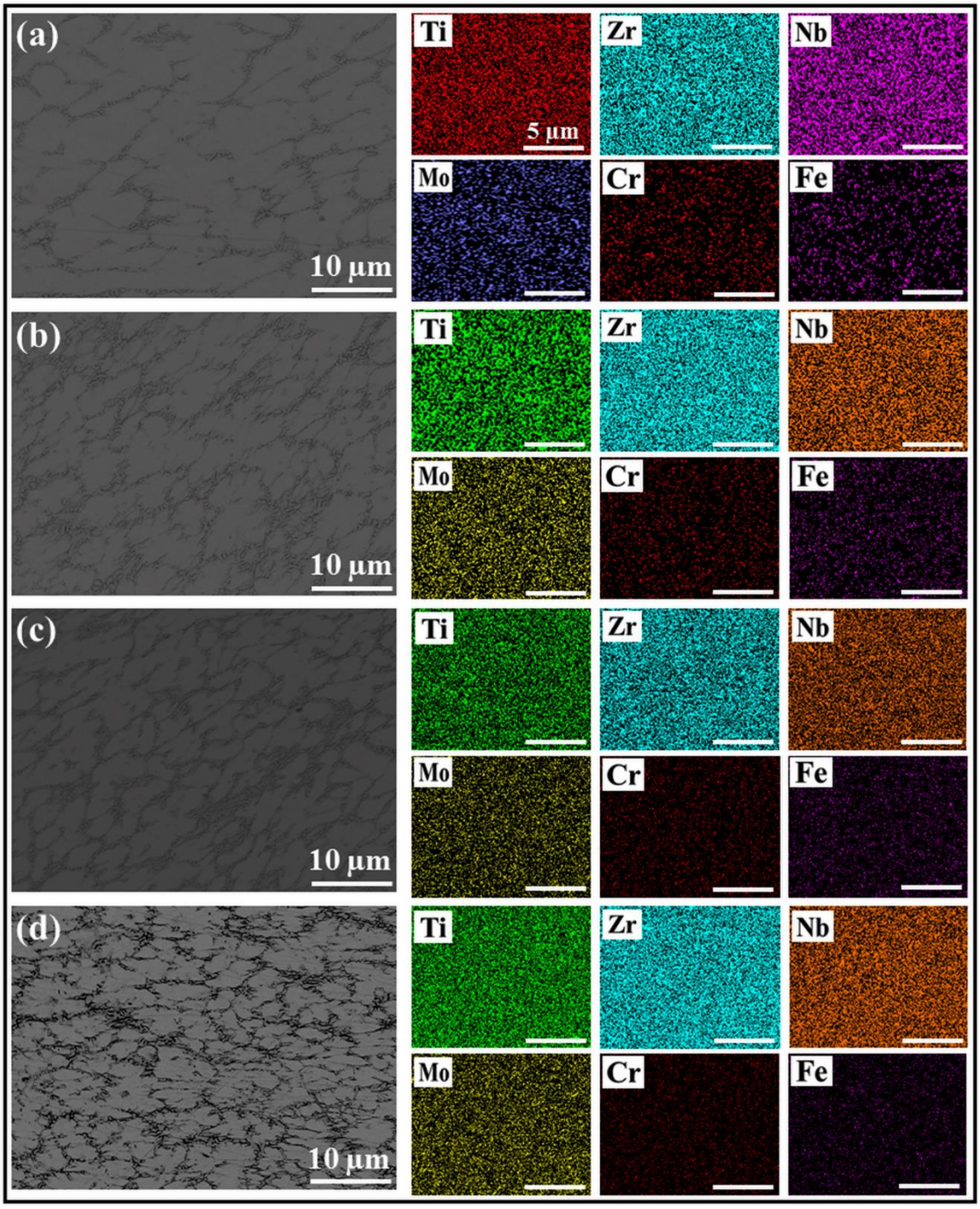

Figure 8.3 SEM images of the HPT-deformed $Ti_{35}Zr_{35}Nb_{15}Mo_5Fe_5Cr_5$ CCA at various number of rotations (a) 1T, (b) 3T, (c) 5T, and (d) 7T, along with the corresponding SEM-EDS elemental mappings.

8.2.2 Mechanical response of the HPT-deformed bio-CCA

The mechanical properties of the HPT-deformed $Ti_{35}Zr_{35}Nb_{15}Mo_5Fe_5Cr_5$ CCA were assessed through instrumented microhardness and Vickers hardness testing. The corresponding results are summarized in Table 8.1 and Figure 8.4. Specifically, Figure 8.4 (a) exhibits the load-displacement curves obtained from the instrumented microindentation. As shown in Table 8.1, the elastic modulus of the HPT deformed CCA, measured by instrumented microindentation, gradually decreases with an increasing number of HPT turns. This reduction in elastic modulus is likely due to the generation of lattice defects, such as dislocations and vacancies, induced by the increasing number of HPT turns.

The elastic modulus of the CCA subjected to HPT deformation decreases from 84.23 ± 4.67 GPa after 1 turn to 68.37 ± 5.16 GPa after 7 turns, as presented in Table 8.1. A similar trend was observed by Edalati et al. for the bio-compatible TiAlFeCoNi HEA [75], where the elastic modulus decreased from 254 GPa in the as-cast condition to 123 GPa after HPT deformation.

Table 8.1. Elastic modulus of the HPT-processed $Ti_{35}Zr_{35}Nb_{15}Mo_5Fe_5Cr_5$ CCA

CCA	**1T**	**3T**	**5T**	**7T**	**as-cast**
Elastic modulus (GPa)	84.23 ± 4.67	76.81 ± 5.09	71.06 ± 2.61	68.37 ± 5.16	97.32 ± 3.58

The variation in Vickers hardness as a function of radial distance from the center of the HPT disc for different numbers of turns is shown in Figure 8.4 (b). The results reveal that the hardness of the HPT-deformed CCA increases with both the number of HPT turns and

the distance from the center toward the edge. A similar trend was reported by Sinha et al. for HPT-processed cp-Ti [238]. The hardness increases rapidly from the center up to a radial distance of approximately 3 mm, beyond which it increases more gradually toward the edge (around 4 mm from the center). This change in the slope of the hardness profile (from center to edge) becomes more pronounced in specimens subjected to higher degrees of deformation, particularly those deformed with 3, 5, and 7 HPT turns.

However, in the sample subjected to 1 HPT turn, the hardness gradually increases from the center to the edge, following an approximately linear trend with a relatively lower slope. This variation in hardness is due to the increasing shear strain with increasing distance from the disc center, as described by Equation 3.2. In addition, the hardness at the central region consistently increases with the number of HPT turns. This behaviour is probably associated with the strain gradient produced during HPT, which leads to the formation of geometrically necessary dislocations (GNDs) [239].

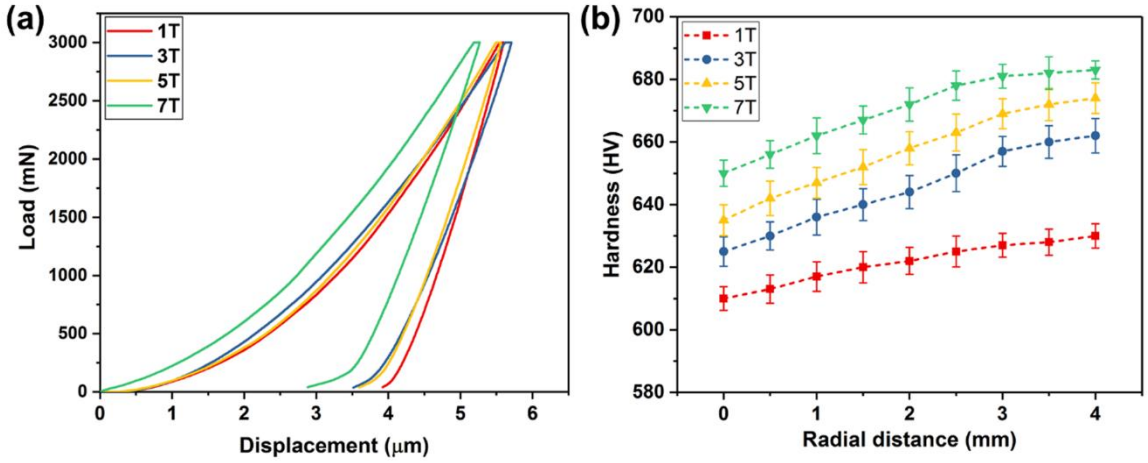

Figure 8.4 (a) Load-displacement curve of instrumented microindentation and (b) Vickers hardness profile of HPT deformed specimens at 1, 3, 5, and 7 turns.

8.2.3 Corrosion behaviour of the HPT-deformed bio-CCA

The potentiodynamic polarization and electrochemical impedance tests were carried out in SBF solution to thoroughly evaluate the corrosion behaviour of the HPT-deformed $Ti_{35}Zr_{35}Nb_{15}Mo_5Fe_5Cr_5$ CCA. Figure 8.5 (a) exhibits the potentiodynamic polarization curve, from which the electrochemical parameters were determined by extrapolation. These values are summarized in Table 8.2. As evident from the table, increasing the number of HPT turns leads to an increase in corrosion potential (from –137.4 mV to –71.6 mV) and a decrease in corrosion current density (from 3.302×10^{-7} to 4.660×10^{-8} A/cm²). The specimen subjected to 7 HPT turns demonstrated the highest corrosion potential (V_{corr}) and the lowest corrosion current density (I_{corr}). Based on electrochemical principles, this combination of higher V_{corr} and lower I_{corr} indicates enhanced corrosion resistance.

Additionally, the corrosion rate of the alloy is directly related to the I_{corr}. As the number of HPT turns increases, the corrosion rate of the CCA decreases significantly, as illustrated in Table 8.2. The corrosion rate of the HPT-deformed CCA is significantly lower than that of the as-cast condition [discussed in Chapter 6], indicating enhanced corrosion resistance after HPT-deformation. Edalati et al. and Song et al. also reported similar observations for HPT-processed $Al_{0.1}CoCrFeNi$ and FeNiCoMoV HEAs, respectively [236,240].

Table 8.2. Electrochemical parameters of the various HPT-deformed $Ti_{35}Zr_{35}Nb_{15}Mo_5Fe_5Cr_5$ CCA specimens in SBF solution.

CCA	Corrosion potential (V)	Corrosion current density (A/cm^{-2})	Corrosion rate (mm/year)

$Ti_{35}Zr_{35}Nb_{15}Mo_5Fe_5Cr_5$ (1T)	- 0.1374	3.302×10^{-7}	3.100×10^{-3}
$Ti_{35}Zr_{35}Nb_{15}Mo_5Fe_5Cr_5$ (3T)	- 0.1197	1.594×10^{-7}	1.496×10^{-3}
$Ti_{35}Zr_{35}Nb_{15}Mo_5Fe_5Cr_5$ (5T)	- 0.0893	9.227×10^{-8}	8.663×10^{-4}
$Ti_{35}Zr_{35}Nb_{15}Mo_5Fe_5Cr_5$ (7T)	- 0.0716	4.660×10^{-8}	4.375×10^{-4}

The electrochemical impedance spectroscopy (EIS) technique is utilized to evaluate the passive film and the interaction between the alloy surface and the physiological electrolyte at the interface. Figure 8.5 (b–d) exhibits the EIS results in the form of Nyquist and Bode plots for the HPT-deformed $Ti_{35}Zr_{35}Nb_{15}Mo_5Fe_5Cr_5$ CCA in SBF, along with the corresponding equivalent electrical circuit (EEC). Table 8.3 summarizes the EEC parameters used to accurately fit the EIS data. In this table, R_s, R_1, and R_2 correspond to the resistances of the SBF solution, the outer porous layer, and the inner barrier layer, respectively, while CPE1 and CPE2 denote the constant phase elements associated with the outer porous and inner barrier layers. Additionally, the standard deviation parameter (χ^2), with values ranging from 10^{-3} to 10^{-4}, indicates a strong agreement between the experimental data and the proposed EEC model, confirming the reliability of the fitting results.

Figure 8.5 (b) presents the Nyquist plots (real vs. imaginary components of impedance) for $Ti_{35}Zr_{35}Nb_{15}Mo_5Fe_5Cr_5$ CCA specimens subjected to varying numbers of HPT turns. All samples show characteristic semicircular arcs with centers positioned below the x-axis. The diameter of these arcs is directly associated with the material's corrosion resistance, with larger diameters indicating a more protective passive film [236]. Notably, as the number of HPT turns increases, the arc diameter increases significantly, reflecting an improvement in the corrosion resistance of the passive film. Among all the HPT deformed

specimens, the sample deformed with 7 HPT turns shows the largest arc diameter, clearly demonstrating the highest corrosion resistance.

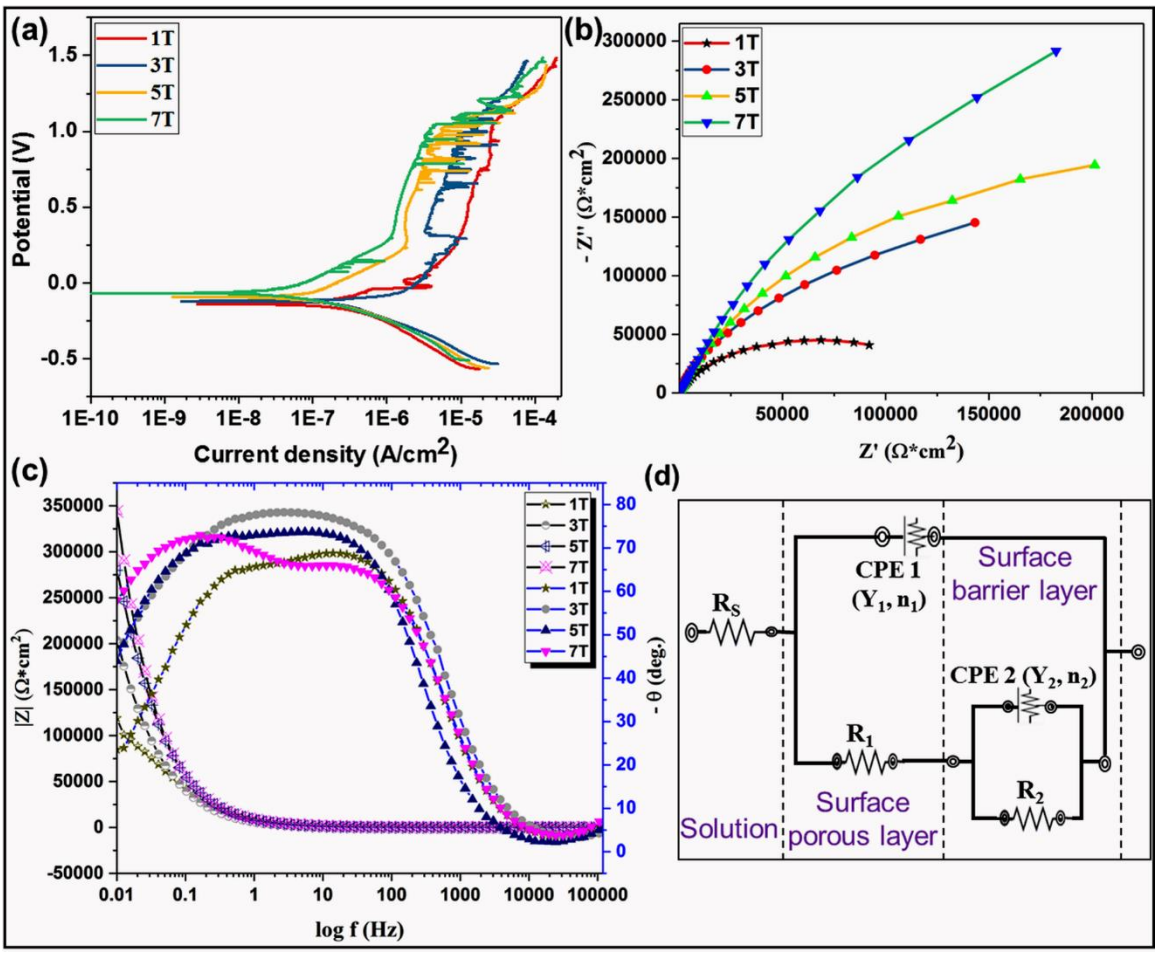

Figure 8.5 Potentiodynamic polarization and EIS spectra of the HPT deformed $Ti_{35}Zr_{35}Nb_{15}Mo_5Fe_5Cr_5$ CCA specimens. (a) Potentiodynamic polarization curve, (b) Nyquist plot, (c) Bode plot, and (d) equivalent electrical circuit (EEC).

Figure 8.5 (c) represents the Bode plots, showing the impedance modulus and phase angle as functions of frequency for the $Ti_{35}Zr_{35}Nb_{15}Mo_5Fe_5Cr_5$ CCA specimens subjected to various turns of HPT deformation. In the high-frequency region, both the impedance modulus and phase angle remain nearly constant, mainly due to the influence of solution resistance. In contrast, as the frequency decreases toward the mid-to-low range, all HPT-deformed

samples exhibit an increase in impedance, a typical indication of the capacitive behavior associated with passive films. Notably, the specimen deformed with 7 HPT turns demonstrates the highest impedance value, reaching approximately 10^5 Ω.cm² at the lowest frequency (10^{-2} Hz), suggesting that the enhanced corrosion resistance is due to the formation of a more protective passive layer in the physiological environment.

Table 8.3 EIS equivalent electrical circuit parameters of the various HPT deformed $Ti_{35}Zr_{35}Nb_{15}Mo_5Fe_5Cr_5$ CCA specimens in SBF solution.

CCA	Rs (Ω cm²)	R_1 (kΩ cm²)	CPE 1		R_2 (kΩ cm²)	CPE 2		χ^2*10^{-3}
			Y_1*10^{-5} (Ω^{-1} cm^{-2} s^{n1})	n_1		Y_2*10^{-5} (Ω^{-1} cm^{-2} s^{n2})	n_2	
$Ti_{35}Zr_{35}Nb_{15}Mo_5Fe_5Cr_5$ (1T)	55.36	8.491	2.028	0.839	129.90	1.076	0.644	1.29
$Ti_{35}Zr_{35}Nb_{15}Mo_5Fe_5Cr_5$ (3T)	79.51	12.980	2.358	0.854	312.83	0.983	0.846	2.83
$Ti_{35}Zr_{35}Nb_{15}Mo_5Fe_5Cr_5$ (5T)	68.49	14.347	1.960	0.884	519.81	0.692	0.706	0.86
$Ti_{35}Zr_{35}Nb_{15}Mo_5Fe_5Cr_5$ (7T)	64.75	15.465	2.027	0.814	1134.90	0.571	0.908	1.10

Figure 8.6 presents SEM images of HPT-deformed CCA samples after a potentiodynamic polarization experiment in SBF solution. The corroded surfaces exhibit evidence of localized corrosion, primarily in the form of small pits. As the HPT turns increases, the number density of these pits decreases. Notably, the sample subjected to 7 HPT turns shows an almost pit-free surface, suggesting significantly enhanced corrosion resistance with greater HPT deformation. This improvement is likely due to the formation of a finer grain structure and a higher density of lattice defects induced by HPT, both of which promote the initiation of a passive oxide layer. Consequently, a denser and more uniform passive film forms on the surface. This trend is further supported by EDS area spectra, which show an increase in oxygen content from 1 to 7 turns, confirming a higher degree of passive oxide formation that contributes to improved corrosion resistance.

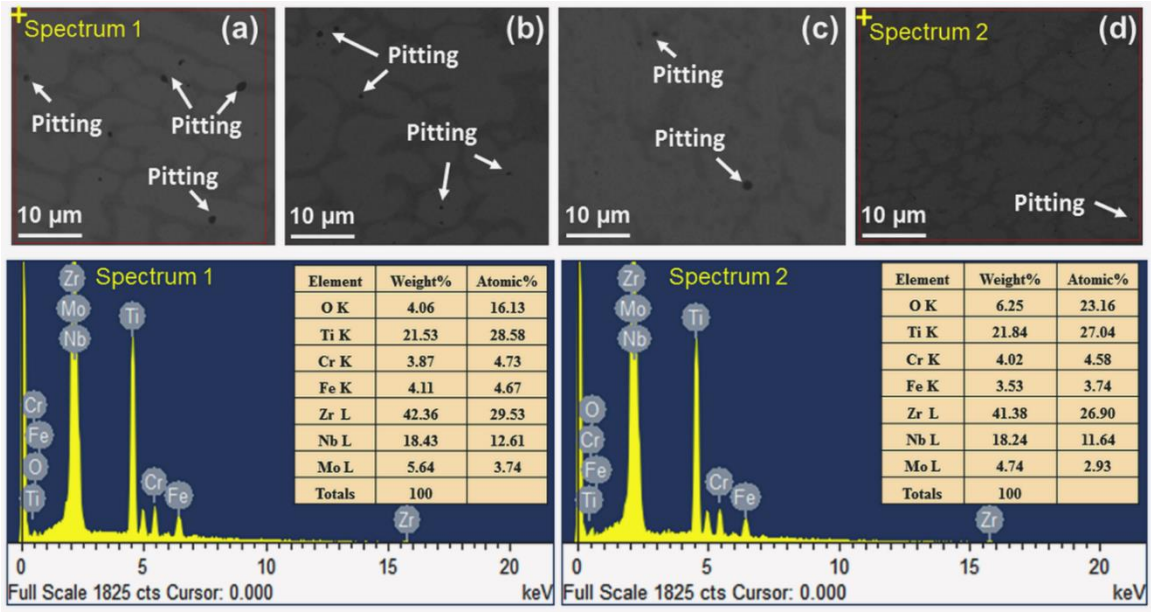

Figure 8.6 SEM corroded surface morphology of the HPT processed $Ti_{35}Zr_{35}Nb_{15}Mo_5Fe_5Cr_5$ CCA at varying number of rotations (a) 1T, (b) 3T, (c) 5T, and (d) 7T. Additionally, spectrum 1 and spectrum 2 are EDS area spectra of the corroded surfaces after 1T and 7T, respectively.

8.2.4 Wetting behaviour of the HPT-deformed bio-CCA

Contact angle measurements were carried out to evaluate the wettability of the HPT-deformed CCA, which reflects the surface characteristics of the alloy, specifically, its hydrophilic or hydrophobic nature. A contact angle below 90° signifies a hydrophilic surface, which is known to facilitate the adsorption of proteins such as fibronectin and vitronectin [241]. As shown in Figure 8.7, all HPT-deformed CCA specimens exhibit contact angles below 90°, confirming their hydrophilic character. Additionally, as the number of HPT turns increases, the contact angle gradually decreases from 58.65° to 50.80°, indicating an enhancement in hydrophilicity. This trend is likely the result of combined factors, including grain refinement, higher surface energy, and improved surface smoothness, all of which contribute to enhanced wettability of the material.

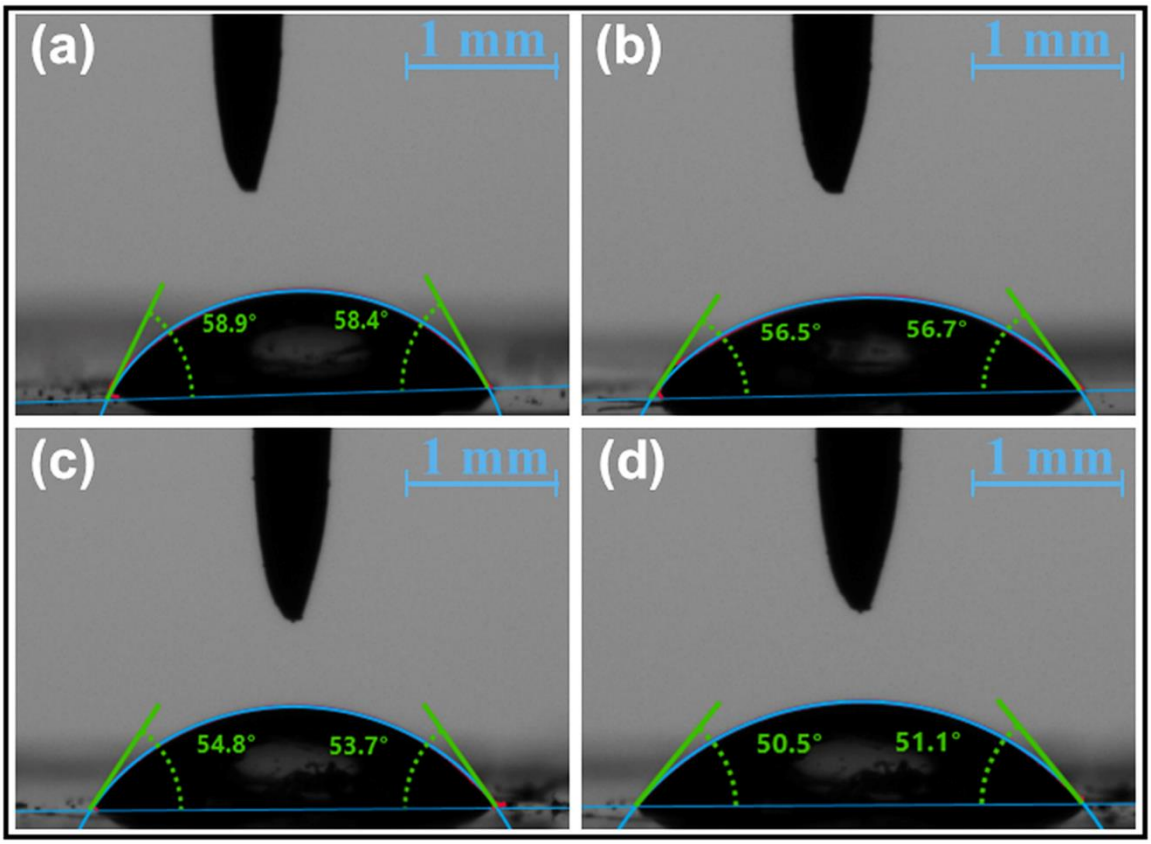

Figure 8.7 Surface contact angle measurement of HPT deformed $Ti_{35}Zr_{35}Nb_{15}Mo_5Fe_5Cr_5$ CCA at varying number of turns (a) 1T, (b) 3T, (c) 5T, and (d) 7T.

8.2.5 In-vitro biocompatibility of the HPT-deformed bio-CCA

The in-vitro biocompatibility of the $Ti_{35}Zr_{35}Nb_{15}Mo_5Fe_5Cr_5$ CCA, including cell adhesion, proliferation, and viability, was assessed using MG-63 cells. Quantitative analysis of the cell culture experiments was carried out using the MTT assay, which measures light absorbance at 590 nm as an indicator of cellular metabolic activity, as shown in Figure 8.8. Notably, higher absorbance values correspond to increased metabolic activity, signifying enhanced biocompatibility. As depicted in Figure 8.8, all HPT-deformed CCA specimens demonstrate significantly enhanced biocompatibility compared to the as-cast CCA (used as the control). Similarly, Floriano et al. reported that HPT deformation enhances the biocompatibility of Ti-based alloys [242].

Additionally, as both the number of HPT turns and the incubation period increase, the absorbance values shown in Figure 8.8 increase accordingly, suggesting improved cell viability and proliferation. Among the CCA samples, the specimen subjected to 7 HPT turns demonstrates the highest levels of viability and proliferation. This improvement is likely attributed to its lower contact angle, which enhances the alloy's wettability and consequently promotes better cell adhesion and proliferation. As reported in Chapter 6, the as-cast $Ti_{35}Zr_{35}Nb_{15}Mo_5Fe_5Cr_5$ CCA exhibited superior biocompatibility compared to both 316L SS and cp-Ti. Therefore, the HPT-processed $Ti_{35}Zr_{35}Nb_{15}Mo_5Fe_5Cr_5$ CCA also exhibits greater biocompatibility than these conventional biomaterials.

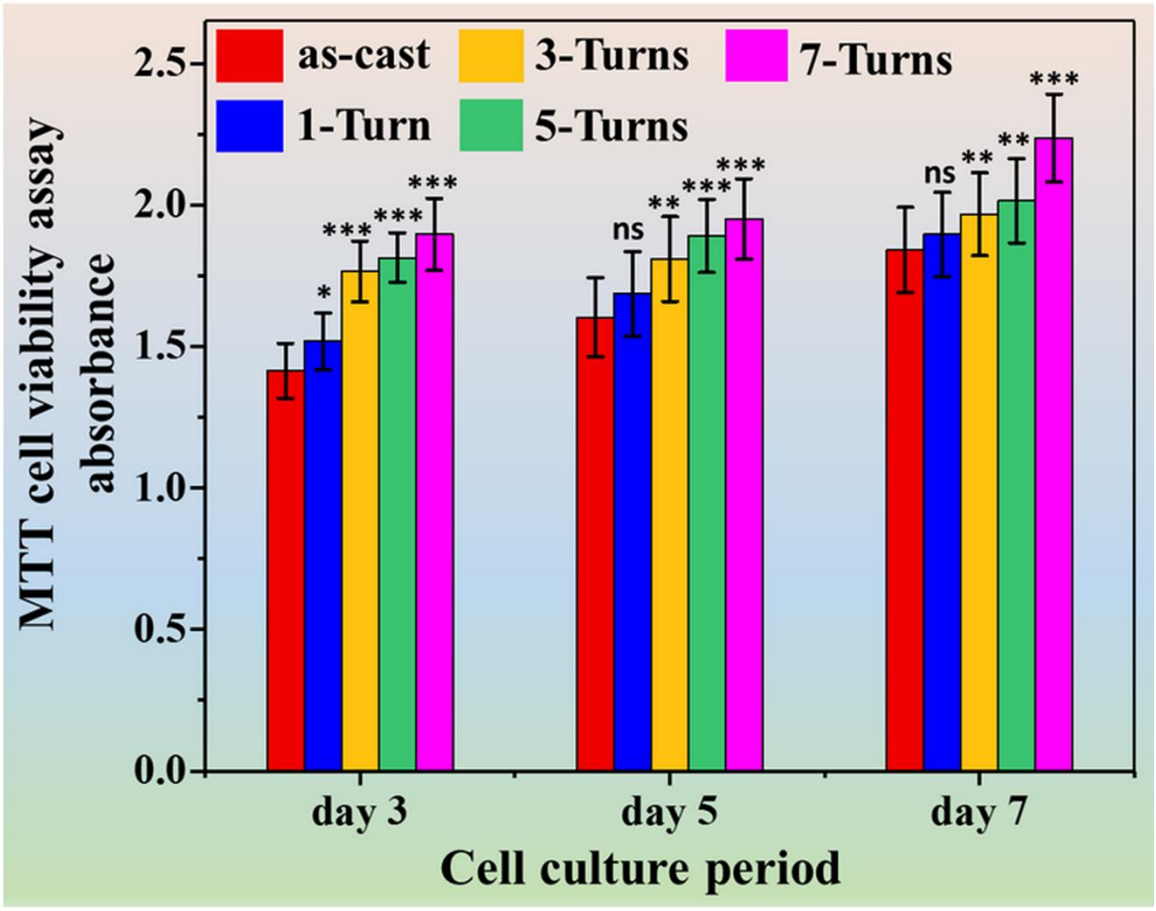

Figure 8.8 MTT cell viability assay illustrating MG-63 cell viability and proliferation of the various HPT deformed $Ti_{35}Zr_{35}Nb_{15}Mo_5Fe_5Cr_5$ CCA specimens after 3, 5, and 7 days of incubation with respect to control (as-cast CCA). Statistical significance was evaluated in relation to the as-cast CCA, with significance levels indicated as: *p < 0.05, **p < 0.01, and ***p < 0.001.

The qualitative biocompatibility analysis, performed using confocal microscopy, reveals the effect of HPT deformation on key biocompatibility parameters, including cell adhesion, morphology, mitochondrial activity, and reactive oxygen species (ROS) generation. Figures 8.9 and 8.10 exhibit confocal images of MG-63 cells adhered to the surface of HPT-deformed $Ti_{35}Zr_{35}Nb_{15}Mo_5Fe_5Cr_5$ CCA after 3 days of incubation, observed using various staining techniques. AO/EtBr staining was used to evaluate cell adhesion and viability, DAPI to observe changes in nuclear DNA morphology, Rhodamine-123 (Rh-123) to monitor mitochondrial activity, and DCFH-DA to detect intracellular ROS levels.

Figure 8.9 shows the confocal microscopy images of the MG-63 cells adhered to the surface of the HPT-deformed $Ti_{35}Zr_{35}Nb_{15}Mo_5Fe_5Cr_5$ CCA at various turns (1T, 3T, 5T, and 7T) after 3 days of incubation stained with acridine orange/ethidium bromide (AO/EtBr). The merged AO/EtBr staining results reveal a substantial number of green-fluorescing (viable) cells adhered to the surfaces of the CCA specimens. These cells show healthy morphologies, characterized by irregular, extended polygonal shapes and a uniform distribution across the surface, indicating enhanced cell migration and proliferation. Notably, there was no evidence of apoptosis or the presence of dead or compromised cells in the HPT-deformed CCA samples. Overall, these findings confirm that the HPT-deformed CCA specimens exhibit excellent cytocompatibility.

DAPI (4',6-diamidino-2-phenylindole) staining was used to evaluate the alterations in the nuclear morphology of MG-63 cells, potentially indicative of apoptosis or necrosis. After three days of incubation, the treated cells maintained their nuclear integrity, with minimal DAPI-positive staining observed (Figure 8.10). These findings indicate the absence of DNA or chromosomal damage. In addition, DAPI staining further confirmed that the CCA specimens maintain good cytocompatibility after HPT deformation.

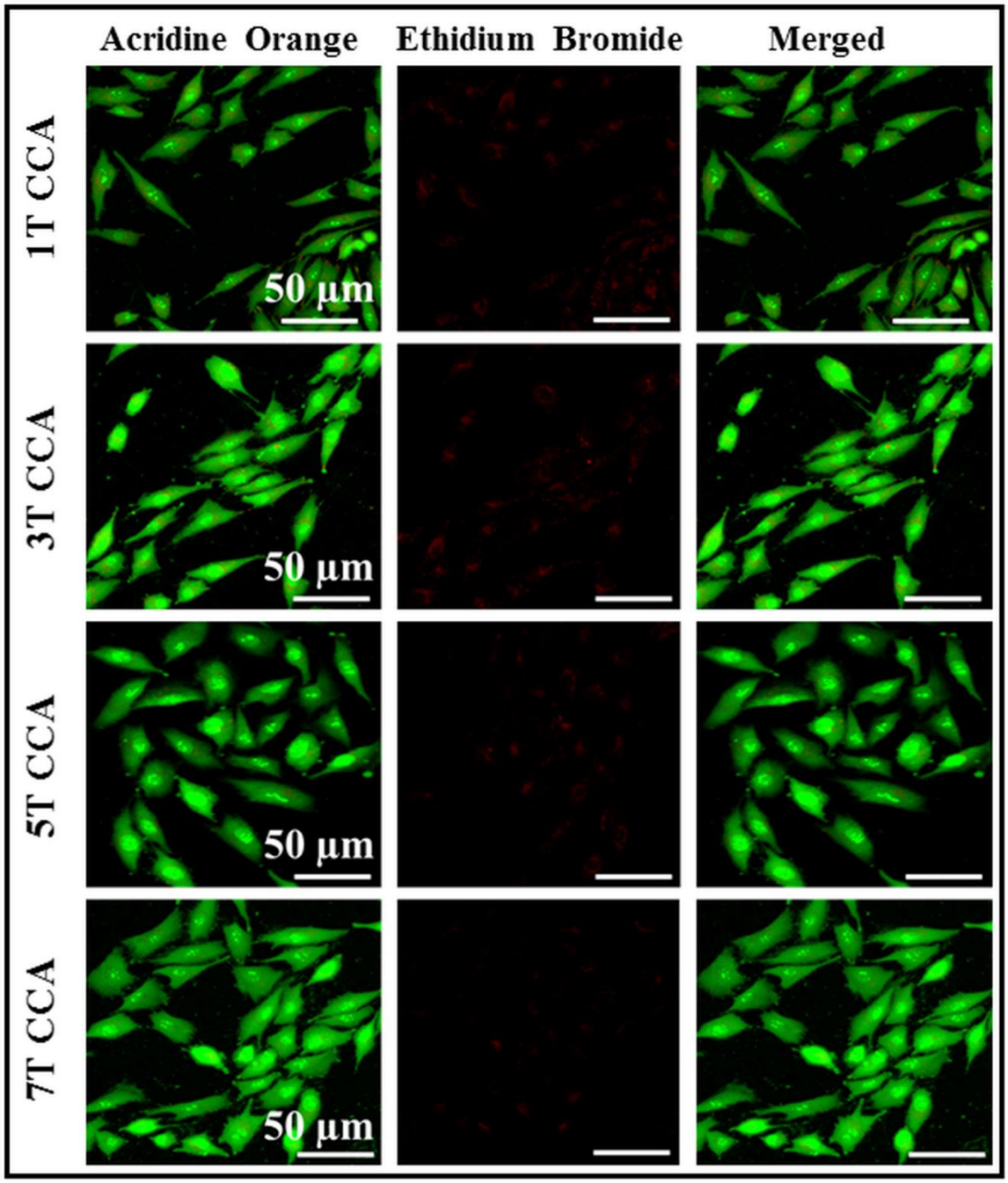

Figure 8.9 Confocal microscopy images of the MG-63 cells adhered to the surface of the HPT-deformed $Ti_{35}Zr_{35}Nb_{15}Mo_5Fe_5Cr_5$ CCA at various turns (1T, 3T, 5T, and 7T) after 3 days of incubation stained with AO/EtBr.

The cytocompatibility of the HPT-deformed CCA was also assessed by analyzing the mitochondrial membrane potential ($\Delta\Psi_m$). For this purpose, MG-63 cell mitochondria were

stained with the fluorescent dye rhodamine-123. Confocal microscopy revealed that both $\Delta\Psi_m$ and rhodamine-123 fluorescence intensity increased with the number of HPT turns, as illustrated in Figure 8.10. These results suggest that HPT deformation significantly improves the cytocompatibility of the $Ti_{35}Zr_{35}Nb_{15}Mo_5Fe_5Cr_5$ CCA through a mitochondria-dependent mechanism, demonstrating superior biocompatibility compared to the as-cast CCA.

DCFH-DA (2,7-Dichloro-dihydro-fluorescein diacetate) staining was performed to assess ROS generation in MG-63 cells cultured on the HPT-deformed CCA sample, and the results illustrated in Figure 8.10. ROS play a critical role in the biological performance of implant biomaterials, as they influence key biological processes such as angiogenesis, cell survival, and energy metabolism [216]. The low green fluorescence intensity observed in the DCFH-DA images indicates minimal ROS production in the HPT-deformed CCA. As reported by Raines et al., lower ROS levels are associated with decreased apoptosis and improved bone formation, fracture healing, regeneration, and osseointegration of implants [216]. These findings further demonstrate that the HPT-deformed $Ti_{35}Zr_{35}Nb_{15}Mo_5Fe_5Cr_5$ CCA possesses superior biocompatibility compared to the as-cast CCA.

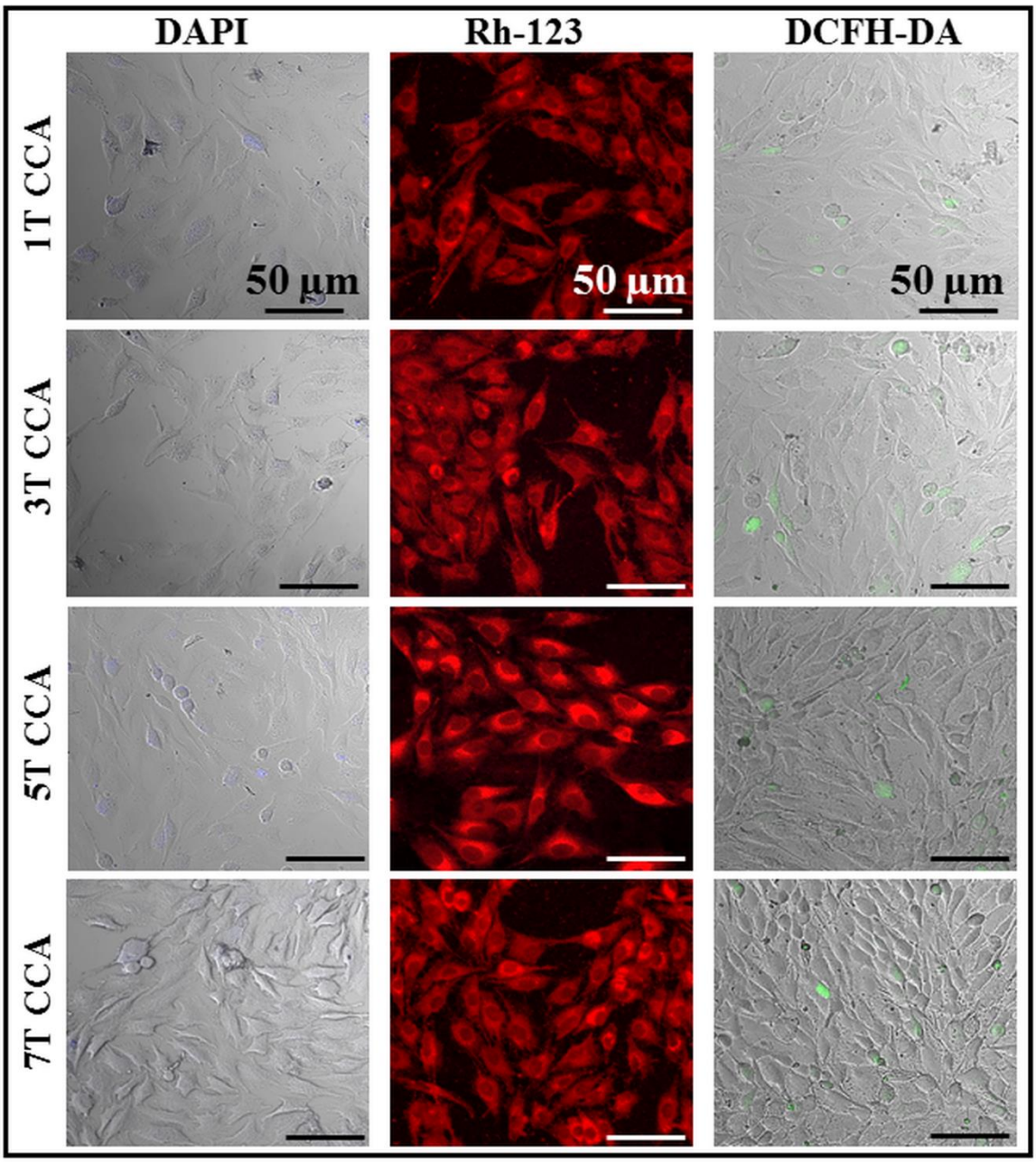

Figure 8.10 Confocal microscopy images of the MG-63 cells adhered to the surface of the HPT-deformed $Ti_{35}Zr_{35}Nb_{15}Mo_5Fe_5Cr_5$ CCA at various turns (1T, 3T, 5T, and 7T) after 3 days of incubation stained with DAPI, Rhodamine-123 (Rh-123, Mitochondria probe), and DCFH-DA.

8.3 Discussion

This chapter illustrated that HPT may be successfully utilized as a processing technique to reduce the elastic modulus of $Ti_{35}Zr_{35}Nb_{15}Mo_5Fe_5Cr_5$ CCA. Moreover, it has a

pronounced effect on the microstructure and significantly improves the associated properties, such as hardness, strength, corrosion resistance, and cytocompatibility of the $Ti_{35}Zr_{35}Nb_{15}Mo_5Fe_5Cr_5$ CCA. The underlying mechanisms, by which HPT influences the microstructural evolution and properties, merit further discussion and are explained below.

HPT deformation is non-uniform plastic deformation, with the degree of plastic strain progressively increasing from the center to the edge of the disc. As calculated using Equation 3.2, the nominal shear strain reaches its maximum at the periphery and is theoretically zero at the center. However, in practice, the center of the disc does experience measurable strain. This deviation arises from the initial application of high compressive stress (4 GPa in this case) prior to torsional deformation, which generates a dislocation-rich stress field and results in non-zero strain at the center [243]. The schematic in Figure 8.11 illustrates the mechanism of microstructural evolution during HPT. The process begins with plastic deformation-induced dendritic fragmentation and dislocation generation, followed by the formation of dislocation cells. These cells then elongate and rotate, eventually transforming into fine-grained microstructure, as described below.

In Stage I (early stage of straining), severe plastic strain leads to the fragmentation of as-cast dendrites, accompanied by the formation of a high dislocation density [244]. In Stage II, the grains become increasingly distorted as dislocations accumulate, forming dislocation tangles and cells within the grain interiors and aligning along the shear direction (SD) [159,245]. This dislocation accumulation also promotes the formation of numerous low-angle grain boundaries. In addition, the high stacking fault energy inherent to BCC-structured refractory-based alloys facilitates dislocation glide, climb, and cross-slip, thereby enhancing dynamic recovery [246]. Consequently, dislocations are annihilated or rearranged, resulting

in a microstructural transformation characterized by the formation of polygonized sub-grains or cellular structures.

As deformation progresses (Stage III), the grains become increasingly elongated along the SD, accompanied by a reduction in the spacing between grain boundaries. Individual grains are further subdivided into multiple sub-grains with similar crystallographic orientations, separated by low-angle grain boundaries. In the final stage (Stage IV), under severe straining, continuous lattice rotation leads to a gradual increase in the misorientation of these sub-grain boundaries. Consequently, many low-angle boundaries transform into high-angle grain boundaries [159]. The formation of new high-angle boundaries, whether through grain subdivision or the evolution of existing low-angle boundaries, ultimately results in the development of a nanocrystalline microstructure.

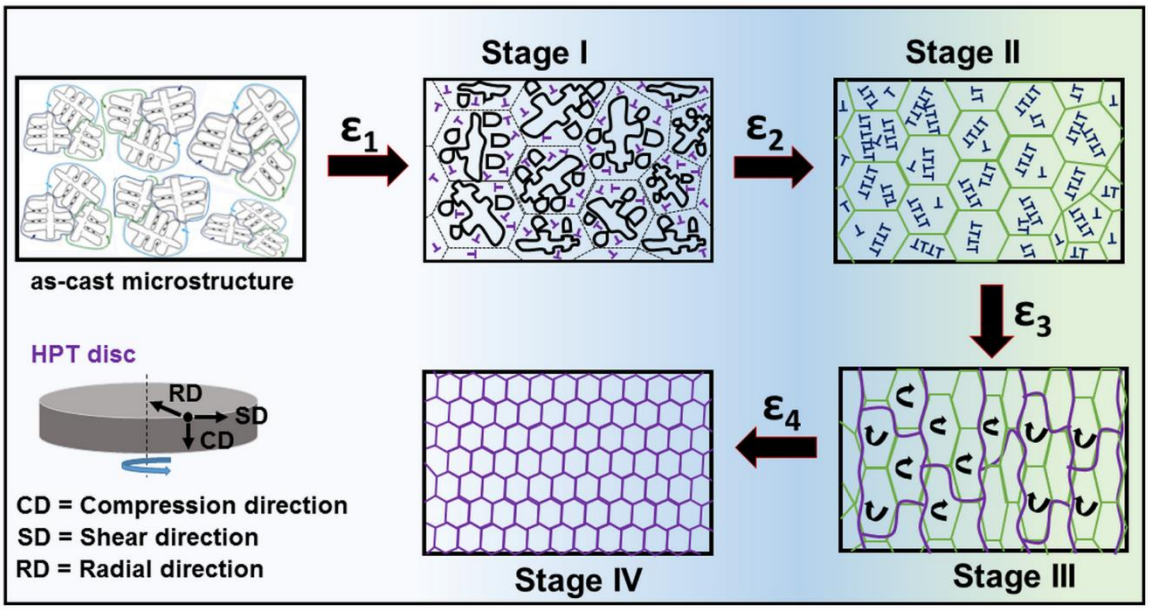

Figure 8.11 Schematic representation of mechanism of the microstructure evolution during HPT (adapted from [159]).

Accordingly, the observed enhancement in corrosion resistance with an increasing number of HPT turns can be attributed to the formation of a nanocrystalline microstructure. This fined-grained structure, enriched with a high density of high-angle grain boundaries and dislocations, provides numerous active sites that facilitate oxide nucleation, thereby promoting the development of a protective passive layer [247-250]. In physiological environments, these structural defects accelerate the oxidation process, promoting the rapid development of a denser passive layer enriched with constituent elements. The nature and quantity of oxides formed within this layer are governed by the chemical reactivity and standard electrode potential of the individual elements. In similar CCA systems, a few studies have reported the formation of stable oxides such as Cr_2O_3, TiO_2, ZrO_2, MoO_3, Nb_2O_5, and Fe_2O_3 [67,69]. These oxides collectively contribute to the formation of a dense, adherent passive layer that effectively shields the alloy surface and significantly improves corrosion resistance.

The biocompatibility of the HPT-deformed $Ti_{35}Zr_{35}Nb_{15}Mo_5Fe_5Cr_5$ CCA was evaluated using cell culture experiments with MG-63 osteosarcoma cells, which demonstrated a significant improvement in cell adhesion and proliferation. This enhancement is primarily attributed to changes in the material's wettability and surface energy, critical parameters governing cell-material interactions. Both properties, evaluated via contact angle measurements, exhibit an inverse relationship with the contact angle: lower contact angles indicate higher wettability (greater hydrophilicity) and increased surface energy [221]. The enhanced wettability and surface energy are a direct result of microstructural refinement induced by HPT deformation. These surface characteristics play a crucial role in promoting protein adsorption and subsequent cellular responses, thereby contributing to the alloy's superior biocompatibility and highlighting its potential for biomedical applications.

In addition, the biocompatibility of metallic biomaterials is closely associated with the leaching of toxic metal ions into the physiological environment. This ion release is directly correlated with the I_{corr}, where higher values indicate increased dissolution [246]. In the present chapter, HPT deformation led to a notable decrease in I_{corr} value, resulting in reduced metallic ion dissolution. This improvement is largely due to the spontaneous formation of a stable, cytocompatible oxide layer on the surface of the CCA, which not only minimizes ion leaching but also supports cell adhesion and proliferation [222,252]. Additionally, the observed trend in corrosion current density shows that the HPT-deformed $Ti_{35}Zr_{35}Nb_{15}Mo_5Fe_5Cr_5$ CCA releases considerably fewer toxic ions compared to its as-cast counterpart and conventional implant materials such as Ti6Al4V, cp-Ti, and 316L SS [251,218]. This reduction in ion release enhances cytocompatibility. Overall, the results demonstrate that HPT deformation does not compromise cytocompatibility while also providing additional advantages such as enhanced mechanical properties, superior corrosion resistance, and a lower elastic modulus. Therefore, the HPT-deformed $Ti_{35}Zr_{35}Nb_{15}Mo_5Fe_5Cr_5$ CCA demonstrates significant potential for biomedical applications.

8.4 Summary

In this chapter, a thorough investigation was carried out on the microstructural evolution, mechanical response (including hardness and elastic modulus), corrosion behaviour, and in-vitro biocompatibility of HPT deformed $Ti_{35}Zr_{35}Nb_{15}Mo_5Fe_5Cr_5$ CCA. The key findings derived from this work are summarized as follows.

i. The HPT-deformed CCA showed a notable refinement in crystallite size, accompanied by a substantial increase in both dislocation density and lattice strain

compared to the as-cast condition. Specifically, the sample deformed up to 7 HPT turns reached a peak dislocation density of 17.50 (±1) × 10^{15} /m^2 and a minimum crystallite size of 8.29 ± 1.10 nm.

ii. The hardness of the HPT-deformed CCA progressively increases from the center toward the edge of the disc, as well as with the number of HPT turns. A notable reduction in elastic modulus was observed after HPT processing, decreasing from 97.32 ± 3.58 GPa in the as-cast state to 68.37 ± 5.16 GPa after 7 HPT turns. This reduction in elastic modulus is primarily attributed to the accumulation of lattice defects, such as vacancies and dislocations, which increase with the number of HPT turns.

iii. HPT deformation notably enhanced the corrosion resistance of the CCA in SBF solution compared to the as-cast condition, with further improvements observed as the number of HPT turns increased. SEM analysis of the corroded surfaces showed that the CCA processed with 1 turn of HPT had fewer corrosion pits than the as-cast sample, while the specimen subjected to 7 turns exhibited an almost pit-free surface. These results indicate that the 7T HPT-deformed CCA develops a strong passive layer that effectively inhibits the release of metallic ions.

iv. In-vitro cell culture evaluations, such as MTT assay, AO/EtBr staining, DAPI staining, Rh-123 staining, and DCFH-DA staining, confirmed that the HPT-deformed CCA exhibits excellent cell adhesion, proliferation, and high cell viability. These results demonstrate the strong potential of the HPT-deformed CCA for biomedical applications.